Metastable austenite driven work-hardening behaviour in a TRIP-assisted dual phase steel

B.L. Ennis [a, b, *], E. Jimenez-Melero [b, c], E.H. Atzema [a], M. Krugla [a], M.A. Azeem [b, d], D. Rowley [b, d], D. Daisenberger [e], D.N. Hanlon [a], P.D. Lee [b, d]

[a] Tata Steel Research and Development, 1970 CA, IJmuiden, The Netherlands
[b] The School of Materials, University of Manchester, Oxford Road, Manchester, M13 9PL, UK
[c] Dalton Cumbrian Facility, Westlakes Science and Technology Park, Moor Row, CA24 3HA, UK
[d] Manchester X-Ray Imaging Facility, Research Complex at Harwell, RAL, Didcot, OX11 0FA, UK
[e] Diamond Light Source Ltd, Diamond House, Harwell Science & Innovation Campus, Didcot, OX11 0DE, UK

A R T I C L E   I N F O

A B S T R A C T

The mechanically-induced transformation behaviour of the metastable austenite phase in a high-strength industrial TRIP-assisted Dual Phase steel was monitored in situ using high-energy synchrotron diffraction under uniaxial loading. This allowed direct quantification of the impact of the transformation of the metastable austenite phase (16 vol %), embedded in a ferrite-bainite-martensite matrix, on the work hardening behaviour of this steel. Our results show that the mechanically induced transformation of austenite does not begin until the onset of matrix yielding. We provide experimental evidence which demonstrates for the first time that the austenite transformation increases the work-hardening contribution, σ_w thereby supporting a driving force approach to transformation induced plasticity. The transformation work required leads to an increase in the macroscopic work-hardening rate after matrix yielding and continues to offset the decrease in the work-hardening rate in the ferrite and martensite phases up to the UTS. Further we show conclusively that martensite yielding does not occur until the completion of the mechanically induced transformation of austenite. Plastic deformation of martensite is immediately followed by local plastic instability leading to necking and ultimate failure of this material.

© 2016 The Authors. Published by Elsevier Ltd. This is an open access article under the CC BY license (http://creativecommons.org/licenses/by/4.0/).

1. Introduction

The automotive sector is currently demanding materials with improved formability and crash performance. The latter property is directly linked to the strength of the material used to absorb the crash energy and withstand intrusion which has in recent years triggered the continuous development of advanced high strength steels (AHSS) with increased levels of ductility and microstructural complexity. The high strength steel development is beginning to differentiate a number of classes of multi-phase (MP) steels based on real world applications in this field (Hofmann et al., 2009). The first generation

AHSS possess primarily ferrite-based microstructures (Matlock and Speer, 2008) and are grouped according to the pre-dominant microstructure type: dual phase (DP), complex phase (CP) and transformation induced plasticity (TRIP).

DP steels are characterised by non-contiguous martensite phase in a relatively soft ferrite matrix, whereby the strength of DP steels is largely dependent upon the relative hardness and volume fraction of the secondary martensite phase (Oliver et al., 2007); mechanical properties are characterised by low yield ratios, continuous yielding, high initial work hardening rates and a good combination of strength and ductility. The DP microstructure is generated by annealing the material in the intercritical ($\alpha + \gamma$) region, where α and γ represent the *bcc* ferrite and *fcc* austenite phases respectively, followed by quenching below the martensite start temperature (M_s), whereby the high-temperature γ-phase transforms to martensite (α') islands, Fig. 1a and c. The advantages of DP steels over conventional high-strength low alloy steels are low yield stress to tensile strength ratios and higher formability (Mazinani and Poole, 2007).

The group of TRIP steels is named after the inherent dominant TRansformation Induced Plasticity effect in those steels. Fischer (Fischer et al., 2000) identified two types of TRIP steel, namely:
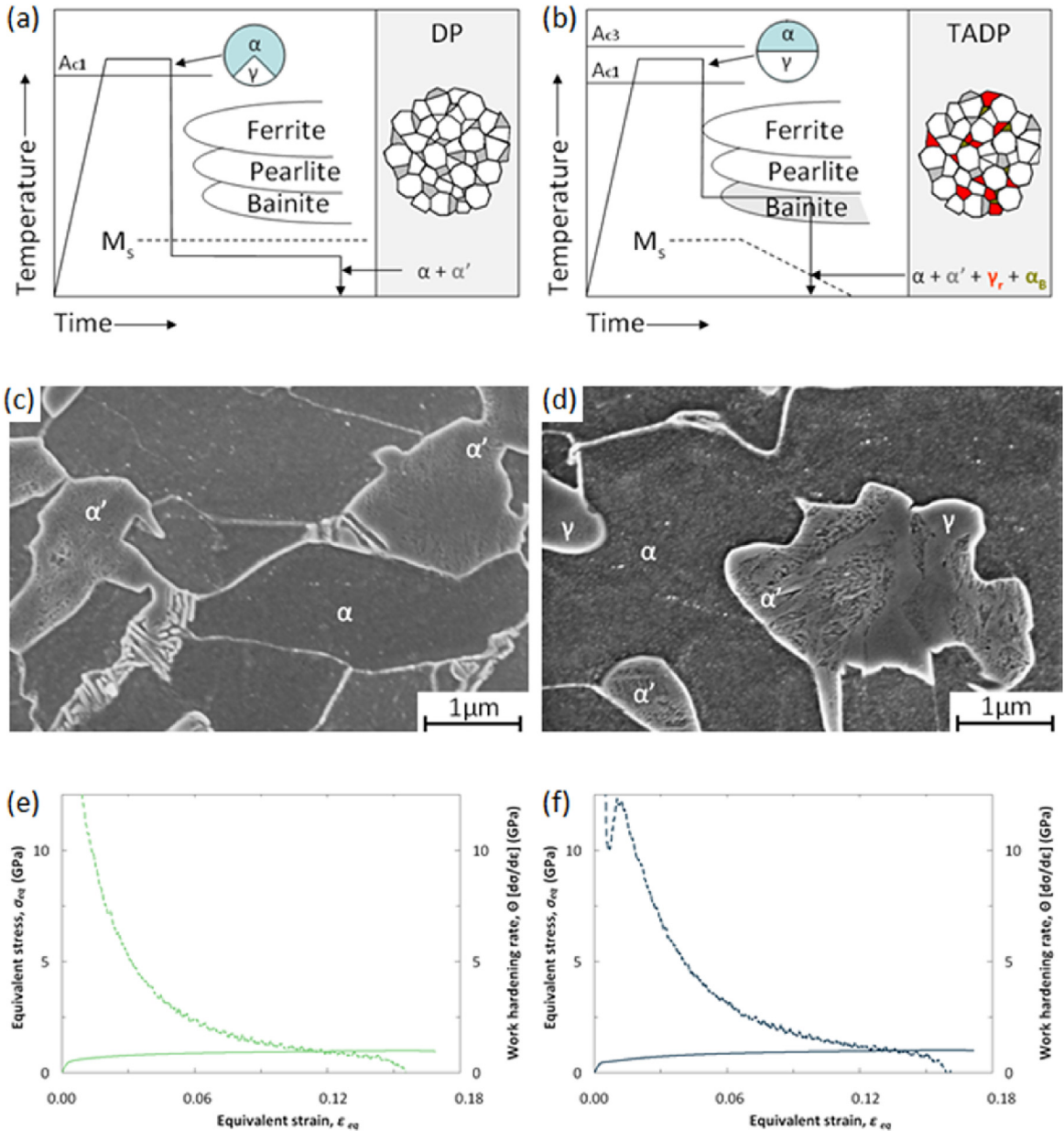

Fig. 1. (a, b) Schematic representation of typical annealing cycles, with (c, d) their final microstructures and (e, f) the equivalent stress and work-hardening rate, Θ, as a function of the nominal equivalent strain of DP (left) and TADP (right) steels.

- High-alloyed Ni-Cr steels characterised by a fully austenitic microstructure at room temperature
- Low-alloyed steel consisting of a ferritic-bainitic matrix, with up to 20 vol% austenite retained in the form of small packets in the parent phase grains or as layers along the grain boundaries.

The latter type of steels is most commonly used for automotive applications, and is produced following an annealing cycle similar to DP steels. The process route in TRIP steels is designed to enrich the austenite phase with carbon, in order to ensure room temperature meta-stability of this phase. This is achieved by introducing an additional processing step in the temperature regime of 300–450 °C, where significant amounts of *bcc* bainite (α_B) form. Due to its limited solubility in the *bcc* lattice, carbon is rejected into the surrounding austenite, thereby enriching it sufficiently that it can be retained in a meta-stable state at room temperature. In order to suppress carbide formation during the isothermal bainitic holding stage, significant additions of other alloying elements such as silicon and aluminium are used (Gomez et al., 2009; Kobayashi et al., 2012; Oliver et al., 2007). Due to the insolubility of those elements in cementite, their diffusion away from the growing cementite nuclei becomes the rate limiting process, leading to retardation of cementite precipitation kinetics (Bhadeshia and Edmonds, 1979). This results in a final multiphase TRIP steel microstructure consisting of ferrite, bainite and dispersed metastable austenite. The presence of the latter confers the steel with enhanced ductility as a result of the mechanically induced transformation of austenite to martensite. At the same time this transformation leads to increased strength via composite strengthening.

Recently, hybrid TRIP-assisted DP (TADP) (Ehrhardt et al., 2004) steels have been developed based on the DP-type microstructure, i.e. ferrite-martensite, but with optimised chemistry and processing parameters in order to retain a relatively small amount of austenite in the microstructure, see Fig. 1b and d. TADP steels belong to the novel ultrahigh strength steel (UHSS) grades presenting ever finer microstructures. UHSS grades can potentially provide yield stress levels of ~550 MPa and ultimate tensile stress values above 1 GPa. Particularly, TADP steels are produced using a route equivalent to the traditional TRIP steel production, but part of the austenite phase present after the bainitic holding stage does transform into martensite during cooling to room temperature, see Fig. 1b. The resultant TADP microstructure therefore comprises ferrite, bainite, martensite and metastable austenite grains; the enhanced ductility is related to the transforming austenite grains upon deformation. However, the impact of the transforming austenite on the work hardening rate, and also on the onset of localised necking and subsequent failure, in these complex fine-grained steels still remains unknown.

There are two explanations for the mechanism of mechanically induced martensitic transformations, typically applied to coarse grained austenitic steels: one focuses on the effect of strain in creating martensitic embryos for aiding the transformation, so called strain-induced transformation (Olson and Cohen, 1975) and the other focuses on the importance of the mechanical driving force, stress-assisted transformation (Patel and Cohen, 1953). Olson and Cohen (1982) proposed the M_s^σ transformation temperature at which the mechanically induced transformation changes from stress-assisted to strain induced mode.

Considerable research effort has been expended in recent years to model the effect of the transformation on the plasticity of the steel. Those taking into account the strain-induced transformation are based on the assumption that the martensite nucleates on shear band intersections generated by plastic deformation Leblond et al. (Leblond et al., 1989), Cherkaoui et al. (2000), Kubler et al. (2011), Khan et al. (2012) and Franz et al. (2013). More recently, Ma and Hartmaier (2015) have developed a thermodynamic model incorporating both stress induced and strain assisted transformation, but which makes the assumption that there is no plastic flow in the martensite phase.

Wolff et al. (2008) developed a stress dependent transformation behaviour of TRIP steels for tension/compression. Geijselaers and Perdahcıoğlu (2009) proposed that in a fully austenitic steel, the start of the martensitic transformation is more accurately described by a stress criterion based on the concept of mechanical driving force, as proposed by Patel and Cohen (1953). Perdahcıoğlu and Geijselaers (2012) further expanded this stress-assisted transformation model to describe transformations in the biaxial stress state. Mahnken et al. (2009) reported a linear dependence of work-hardening on martensite volume fraction in a low alloy TRIP steel and Ramazani et al. (2013) further reported that by incorporating GNDs in the model improved prediction of work-hardening behaviour. This fits well with the findings of Jacques et al. (2001) who used acoustic emission spectroscopy to derive the dislocation density generated within ferrite by the mechanically induced martensitic transformation, which was shown to be proportional to the incremental work-hardening exponent. Han et al. (2004, 2008) presented similar results by using a combination of *ex-situ* X-ray diffraction and microstructural analysis and Miyamoto et al. (2009) investigated the effect of martensite morphology on local strain distributions in an austenite matrix due to accommodation of the shape strain associated with formation of martensite. This work was carried out on a fully austenitic stainless steel using in situ EBSD, which is unsuitable for low alloy TRIP steels due to the transformation of a large portion of the available austenite during polishing (Aarnts et al., 2011).

In this work, we have employed in situ high energy X-ray diffraction, supported by ex situ local microstructural analysis using scanning electron microscopy, to probe the changes in the constituent phases in a TADP steel during deformation, and therefore assess the impact of the austenite transformation into martensite on the work hardening behaviour and plastic instabilities associated to necking in this material.

Table 1
Chemical composition, mechanical properties and phase fractions of the test steels.

Material	Chemical composition in wt%						Tensile properties				Volume fraction		
	C	Mn	Al	Si	Cr	Fe	σ_y MPa	UTS MPa	A_u %	A_{tot} %	f_α %	$f_{\alpha'}$ %	f_γ %
DP800	0.13	2.04	0.03	0.25	0.55	bal.	534	857	12.1	18.3	88	12	–
TADP800	0.15	2.05	0.55	0.42	0.40	bal.	385	890	14.1	18.9	78	6	16

Table 2
Experimental values of the lattice parameter of ferrite (α) austenite (γ) prior to loading, together with their characteristic mechanical properties in TADP800 steel.

A_α (Å)	a_γ (Å)	$\varepsilon_{y[\alpha]}$	$\sigma_{y[\alpha]}$ (MPa)	$\varepsilon_{y[\gamma]}$	$\sigma_{y[\gamma]}$ (MPa)	$\varepsilon_{y[\alpha']}$	$\sigma_{y[\alpha']}$ (MPa)	ε_{UTS}	σ_{UTS} (MPa)
2.8679	3.6021	0.003	389	0.012	493	0.059	865	0.131	1014

2. Experimental

2.1. Initial microstructure: production and analysis

The steel under investigation is a continuously-cast TRIP assisted dual phase steel, namely TADP800 steel, with the composition given in Table 1. After casting the steel is hot- and cold-rolled followed by continuous annealing designed specifically to suppress the formation of banding (Ennis et al., 2016). A commercial DP steel, namely DP800, was added for comparison, see Table 1. The relative phase fractions in the produced microstructures were determined using metallographic and X-ray diffraction (XRD) analysis. Light microscopy combined with colour etching with Le Pera etchant was complementarily employed to determine the combined second phase fraction, $f_{\alpha'+\gamma}$. The XRD patterns were recorded in the range of $2\theta = 38-165°$, in a fully automated Panalytical Xpert PRO diffractometer operating in reflection mode using Co Kα-radiation. Rietveld refinement of the XRD patterns was performed using the Bruker TOPAS software package (Bruker AXS GmbH, 2009).

2.2. Macroscopic mechanical behaviour

Bulk tensile properties of both materials were measured on a standard tensile test piece with 50 mm gauge length according to EN ISO 6892-1 (The International Organisation for Standardisation (ISO, 2009)). Samples were loaded at a constant strain rate of 5×10^{-3} s^{-1} using an Instron 100 kN tensile tester. The relevant tensile properties are given in Table 1, whereas the graph of equivalent stress *vs.* equivalent strain is shown in Fig. 1e and f. The work-hardening rate, $\Theta = d\sigma/d\varepsilon$[1], as a function of the nominal equivalent stress is also shown for each material in Fig. 1. The data was smoothed using a 5 point quadratic polynomial filter for n (x_j, y_j) points ($j = 1, \ldots n$) (Savitzky and Golay, 1964):

$$Y_j = \sum_{i=-(m-1)/2}^{i=(m-1)/2} C_i y_{j+i} \text{ and } \frac{m+1}{2} \leq j \leq n - \frac{m-1}{2} \tag{1}$$

The yield stress of the individual phases was derived from the work-hardening rate, on the basis of a mixture model (Bergström, 1970; van Liempt, 1994). The resultant values are given in Table 2. An initial series of ex situ (interrupted) tensile tests were also carried out to determine the progression of retained austenite to martensite for the TADP800 material. In these ex situ tests the samples were loaded in intervals of approximately 2% plastic strain up to failure. The retained austenite fraction (f_γ) was measured in the unloaded condition and after each of the interrupted test points by X-ray diffraction.

2.3. In situ high energy X-ray diffraction

High energy synchrotron X-ray diffraction (HE-SXRD) measurements were performed in situ during uniaxial loading on the I15 beamline at Diamond Light Source. The dog-bone TADP steel sample had a gauge cross-section of 0.8×0.6 mm^2. The sample was mounted in a micro-tensile rig installed in the translation/rotation table of the beam line, see Fig. 2a. The sample was oriented such that the load was applied along the rolling direction of the TADP material. The sample was progressively loaded at small strain intervals up to 2.2% plastic strain, see inset of Fig. 2b. At each strain step the sample was illuminated by a monochromatic ($\lambda = 0.1722$ Å) X-ray beam with a spot size on the sample of 70×70 μm^2. The sample was rotated around its

---

[1] Note that in this manuscript the work-hardening coefficient is denoted by the capital Greek letter theta (Θ), to distinguish it from the Bragg diffraction half-angle (θ).
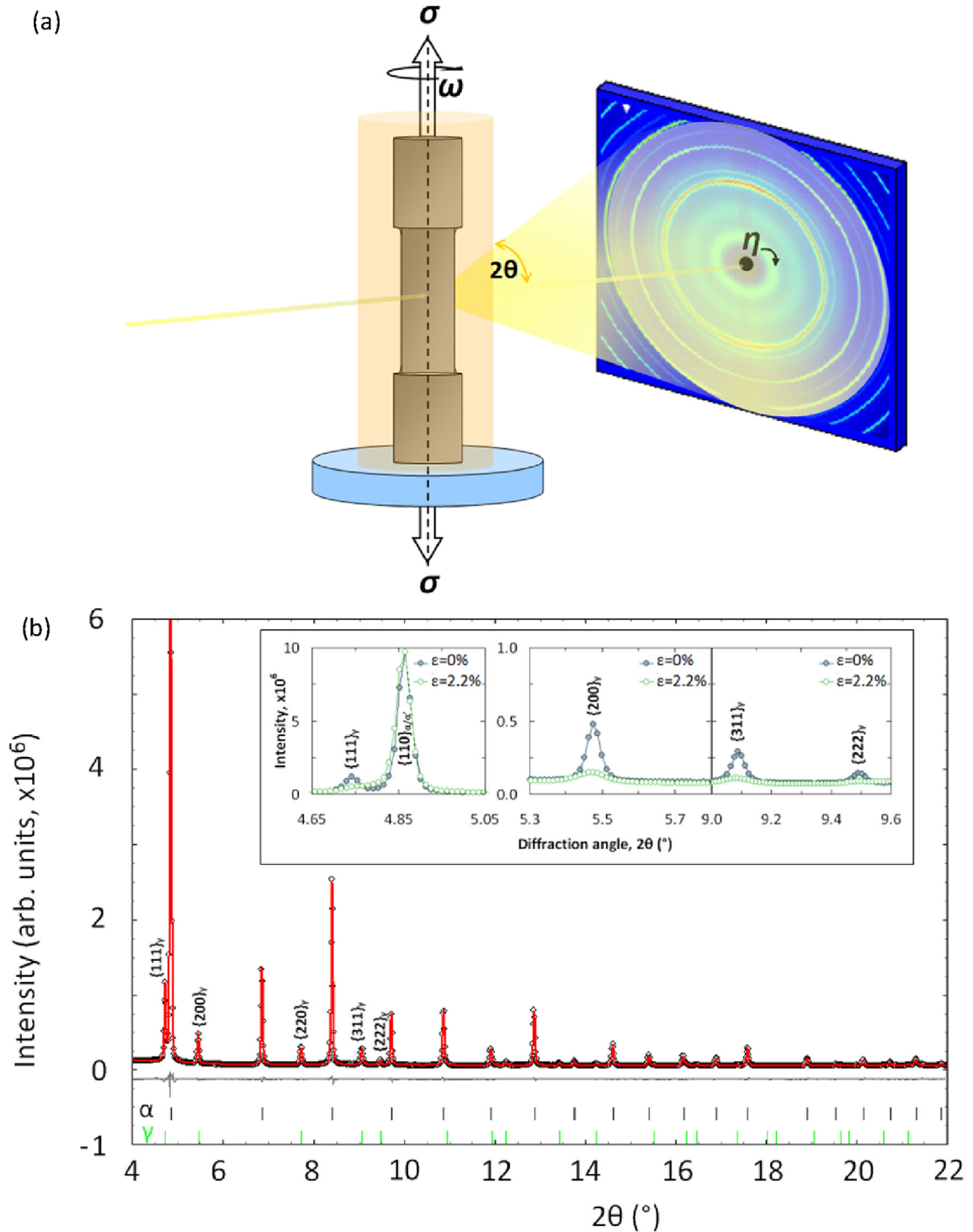
(a)

(b)

Fig. 2. (a) Schematic representation of the HE-SXRD setup used for the in situ X-ray diffraction experiments in transmission geometry under uniaxial loading. (b) Representative 1-D HE-SXRD pattern after indexing and Rietveld refinement. The measured data are given as open black circles, whereas and the fitted pattern is shown in red. The principal austenite reflections are indicated. The inset shows the progression of the selected austenite reflections $(111)_\gamma$, $(200)_\gamma$, $(311)_\gamma$ and $(222)_\gamma$ after 2.2% nominal strain (open green circles) as compared to the unloaded condition (closed blue circles). (For interpretation of the references to colour in this figure legend, the reader is referred to the web version of this article.)

longitudinal axis at constant angular velocity (ω-rotation) and continuous recording of the X-ray diffraction signal using a Perkin-Elmer flat panel CCD detector placed behind the sample. A total ω-range from $-45°$ to $45°$ was recorded for each value of applied strain. The signal was summed per 5° of angular rotation of ($\Delta\omega = 5°$), with a corresponding exposure time for each

recorded diffraction pattern of 15s. The instrumental parameters were obtained using the LaB_6 standard, NIST660b (NIST, 2010).

The measured data set consisted of a series of 2-D diffraction patterns as a function of straining step and ω angle. All the 2-D diffraction patterns recorded at each straining step were summed. Afterwards, integration over the azimuthal angles at constant scattering angle was performed using the FIT2D software package (Hammersley et al., 1996), in order to obtain the corresponding one-dimensional (1-D) intensity vs. scattering angle (2θ) patterns. Rietveld refinement of the resulting 1-D patterns was performed using the Bruker TOPAS software package, in order to determine the phase fraction and lattice parameter of the constituent phases as a function of strain. In this work the terms stress and strain are used to denote the equivalent nominal (or macroscopic) stress and strain, unless otherwise specified.

In addition to the study of the average phase behaviour, we also studied the effect of orientation with respect to the loading direction on the relative change in lattice parameter. Grains where the normal to the scattering planes is favourably oriented along and perpendicular to the loading direction can be isolated by analysing a corresponding angular section on the 2-D detector. A mask was generated to obtain the 1-D spectra in the relevant zones of the 2-D patterns, thereby allowing integration at a constant scattering angle along the longitudinal and transverse directions over $\pm 7.5°$ in azimuthal angle i.e. where the scattering vector is approximately parallel ($\parallel$) or perpendicular ($\perp$) to the loading (and in this case also the rolling) direction of the material, respectively. Furthermore, a fit of individual reflections to a pseudo-Voigt profile function was used to study the diffracted intensities from the grain subsets having specific *{hkl}* plane normals oriented along and perpendicular to the loading direction.

2.4. Local microstructural analysis

Orientation contrast imaging was performed in the unloaded condition, immediately prior to necking, and at fracture in the TADP material. For this purpose, we used a Zeiss Ultra 55 FEG-SEM Ultra Plus at a 15 kV accelerating voltage, followed by EBSD analysis of selected areas using a Hikari camera. The frame rate of the camera was 30 fps, and the scanning step size was 50 nm. A finer step size of 30 nm was used to improve phase quantification. The EBSD maps obtained were analysed using the TSL OIM Analysis software. Kernel average misorientation (KAM) was calculated with respect to the third nearest neighbours.

3. Results and discussion

3.1. Microstructure before loading

Typical unstrained microstructures of both steels are displayed in Fig. 1c and d. They show similar ferrite (α) grain size and second phase fractions ($f_{\alpha'+\gamma}$), see Table 1. In the DP steel, the second phase consists of a network of non-continuous martensite (α') with a lath packet structure. The second phase in the TRIP-assisted DP steel is similar to the DP steel with the addition of blocky austenite (γ) packets, generally, but not always, associated with martensite. Fig. 2b shows a representative 1-D diffraction pattern after indexing of the principal reflections ascribed to the *bcc* ferritic matrix ($\alpha + \alpha_B + \alpha'$) and the *fcc* austenite (γ) phase, and the Rietveld refinement of the whole pattern. The experimental value of the lattice parameter of the phases before loading can be found in Table 2. At room temperature, the lattice parameter of austenite depends upon the chemical composition as follows: (Van Dijk et al., 2005; Scott and Drillet, 2007):

$$a_\gamma = 3.556 + 0.0453x_C + 0.00095x_{Mn} + 0.0056x_{Al} \qquad (2)$$

where a_γ is the austenite lattice parameter in Å and x_C, x_{Mn} and x_{Al} are the alloying concentrations in wt.%. Other elements present in this steel (Si, Cr and P) have negligible effect on the lattice parameter of austenite. The average carbon content in austenite at room temperature is calculated to be 0.90(2) wt.%.

3.2. Austenite transformation during loading

Deformation leads to a progressive reduction in intensity of the austenite reflections, and a concomitant increase in intensity of the reflections from the ferritic matrix, see inset of Fig. 2b. This implies that part of the metastable austenite transforms into martensite under loading. This is most clearly illustrated in the case of the $\{111\}_\gamma$ reflection, where the reduction in intensity is coupled with an increase in the intensity and also in the asymmetry of the low-2θ shoulder of the adjacent $\{110\}_\alpha$ reflection. As previously reported, no additional reflections are observed in the diffraction patterns due to the newly formed martensite phase, which manifests itself rather as an increase in intensity of the *bcc* Bragg reflections (Jimenez-Melero et al., 2007, 2011). Therefore, the ferritic (α) matrix is considered to comprise of intercritical ferrite (α), bainite (α_B) and martensite (α').

Fig. 3 shows the continuous equivalent stress-equivalent strain curve of the TADP800 steel, compared with that of the DP800. The difference in mechanical responses of the two materials becomes more apparent when the stress is plotted logarithmically against the strain rather than linearly (as shown in the inset of the figure); this will be discussed in more detail later. The dashed lines represent the nominal strains from Table 2 at the yield stress and ultimate tensile strength (UTS) of the TADP800 material. The data points on the TADP curve (open diamonds) represent the X-ray diffraction measurements at
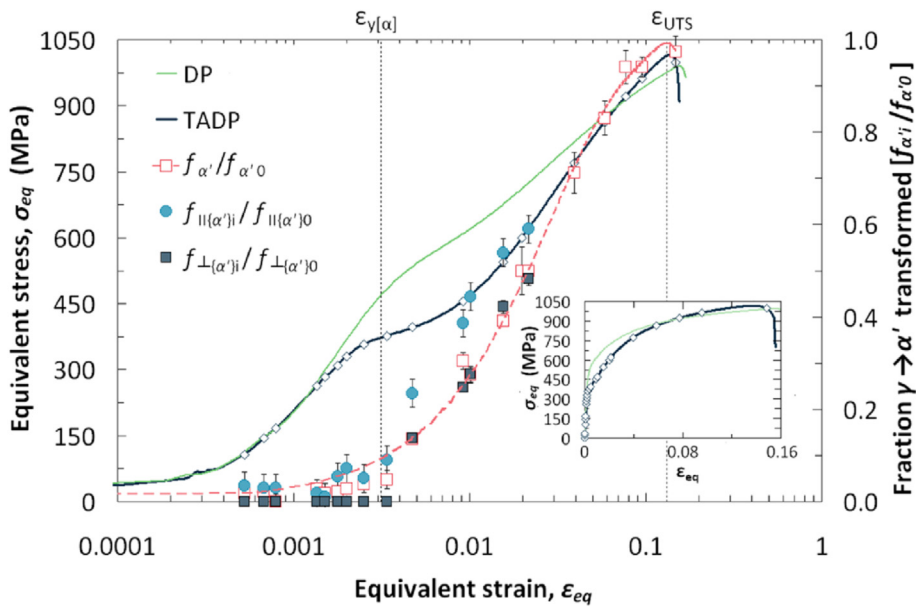
Fig. 3. Relationship between the mechanically-induced transformation of austenite to martensite (red open squares) to the nominal strain in a TRIP-assisted DP steel. The stress of DP800 (solid green line) and TADP800 (solid blue line) are plotted logarithmically and (inset) linearly against strain for comparison. XRD measurements (open diamonds) are indicated along the stress-strain curve of TADP800. The fractions of martensite transformed from retained austenite as function of strain are also shown for the longitudinal (light blue closed circles) and transverse (dark blue closed squares) loading directions. (For interpretation of the references to colour in this figure legend, the reader is referred to the web version of this article.)

constant macroscopic strain. The fraction of austenite which has transformed to martensite is shown as derived from the summed diffraction patterns, and also from the longitudinal and transverse directions. From these data, it can be seen that the transformation of austenite to martensite does not begin until close to the yield strain of the ferrite.

At this yield point there is no transformation in the transverse direction and only 9% transformed in the longitudinal direction, with a total in the whole sample of less than 5% of the initial austenite. Once the surrounding ferritic matrix has started to yield, the mechanically induced austenite to martensite transformation progresses in both grain subsets. The polynomial fit to the bulk measured data (red dashed line) is shown for indication purposes, as the data could not be fitted adequately using a simple logarithmic or linear progression, which indicates that the progression of the TRIP effect is not simply dependent on the nominal strain.

3.3. Load partitioning

During deformation, the load is distributed between the phases present in the evolving microstructure. The average phase behaviour is given by the relative change in lattice parameter obtained through Rietveld analysis of the one-dimensional diffraction patterns. Grains with their plane normal roughly parallel to the loading direction are in a tensile condition, whereas those with their plane normal perpendicular to the applied load are in compression. To distinguish the response of the different grain subsets, selected regions of the 2-D diffraction patterns have been analysed, see experimental section. Fig. 4a and b shows the relationship between lattice plain strains for the ferritic matrix and the austenite phase respectively with the nominal stress. In the case of austenite, the relative change in lattice parameter originates from two contributions: the elastic lattice strain and a change in average carbon content caused by preferential mechanically induced martensite formation from lower carbon content austenite grains. These contributions can be separated by comparing relative changes in lattice parameter in the longitudinal and transverse orientations, since the carbon enrichment has an isotropic effect. The orientation dependence for the elastic strains is defined by the austenite Poisson ratio of $v = 0.367$ ((Adams et al., 2006; Blondé et al., 2012). The relative change in lattice parameter due to carbon enrichment ε_c is given as[2]:

---

[2] The total strain in the austenite phase is the sum of the lattice strain and the isotropic strain due to the carbon content of the austenite remaining at each strain step after transformation. The total lattice strain in the longitudinal (II) and transverse directions are ($\perp$), respectively: $\varepsilon_{II} = \varepsilon_{II}^\sigma + \varepsilon_c$ and $\varepsilon_\perp = \varepsilon_\perp^\sigma + \varepsilon_c$. Given that in a uniaxial tensile test there is no applied transverse stress and assuming that there is no compressive strain constraining the transformation (P = 0), then: $\varepsilon_{II}^\sigma = \frac{\sigma}{E}$ and $\varepsilon_\perp^\sigma = -v\frac{\sigma}{E}$. It follows that since $\varepsilon_\perp^\sigma = -v\varepsilon_{II}^\sigma$, then $\varepsilon_c = \frac{\varepsilon_\perp + v\varepsilon_{II}}{1+v}$, which is identical to Eq. (3).
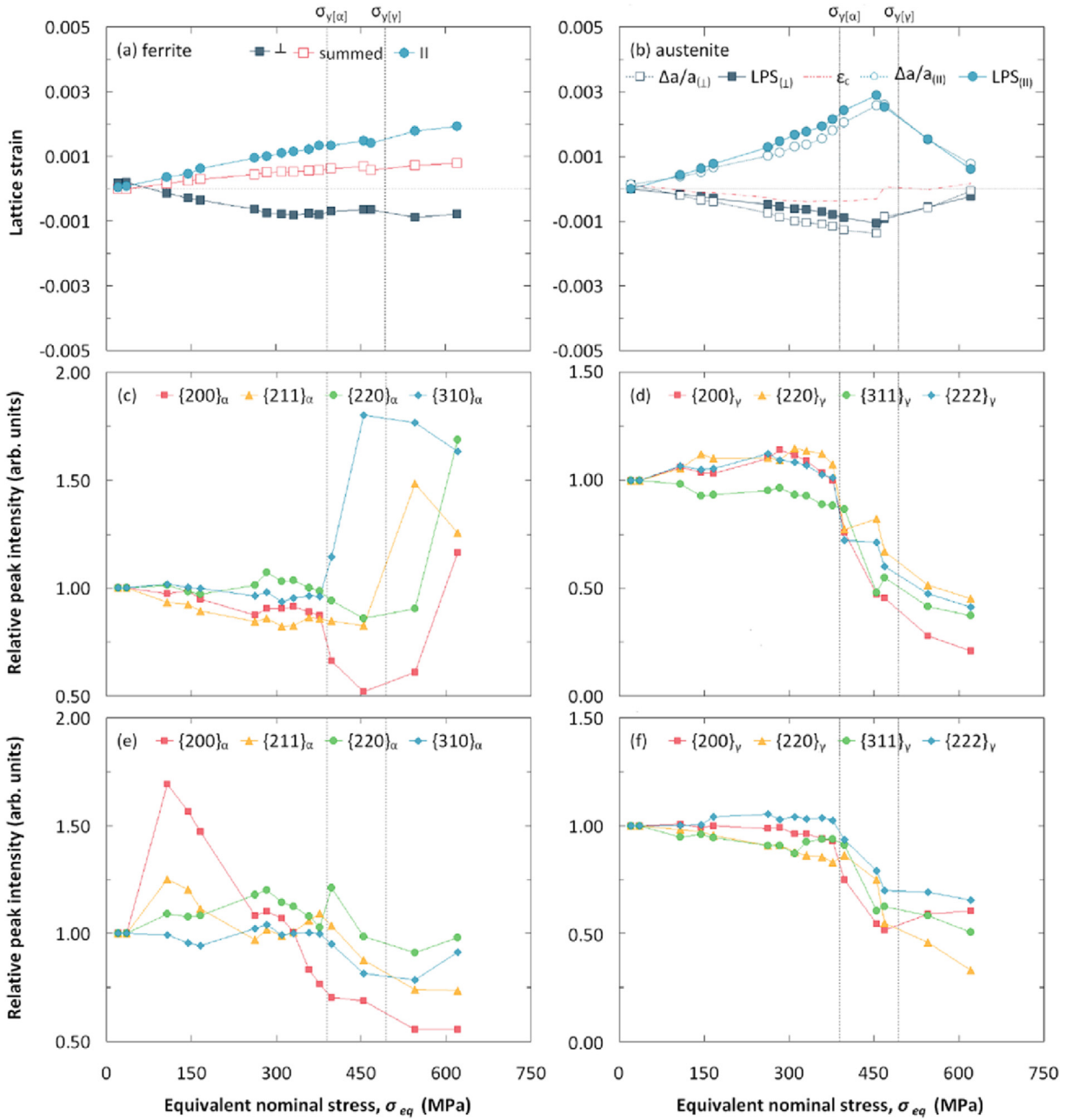
Fig. 4. Lattice plane strain in (a) ferrite and (b) austenite as a function of nominal stress. For austenite the open symbols correspond to the relative change in lattice parameter which is due to the sum of the elastic strain and carbon enrichment. The closed symbols represent the stress contribution to the lattice strain. These contributions have been separated by using the Poisson ratio for austenite[§]. The effect of carbon enrichment (ε_c) is indicated by the red dashed line. Relative peak intensity as a function of the nominal stress in (c, e) ferrite and (d, f) austenite grains with plane normals oriented (c, d) parallel to the loading direction (II) and (e, f) perpendicular to the loading direction (⊥). The vertical dashed lines indicate the yield stresses of ferrite ($\sigma_{y[\alpha]}$) and austenite ($\sigma_{y[\gamma]}$) phases in the TADP steel, as calculated from the second derivative of the work-hardening curve (see Table 2 and Fig. 6). (For interpretation of the references to colour in this figure legend, the reader is referred to the web version of this article.)

$$\varepsilon_c = \frac{\left[\left(\frac{\Delta a_\perp}{a}\right) + \nu\left(\frac{\Delta a_\parallel}{a}\right)\right]}{(1 + \nu)} \tag{3}$$

where $\frac{\Delta a_\parallel}{a}$ and $\frac{\Delta a_\perp}{a}$ are the relative changes in lattice parameter for the longitudinal and transverse orientations respectively, as indicated by the open symbols in Fig. 4b. The lattice plane strains in the longitudinal and transverse directions are obtained by

subtracting ε_c from the relative change in lattice parameters. The resulting value of ε_c is indicated in Fig. 4b by the dashed line and the lattice plane strains (LPS) by the closed symbols.

Fig. 4a and b shows a linear stress-lattice strain response of both phases until the yield point of ferrite ($\sigma y_{[\alpha]}$) above which the austenite phase begins to deviate significantly from this trend. This deviation indicates the onset of phase yielding at ~460 MPa as indicated by the inflection in the strain data. This is in reasonable agreement with the yield point derived from the macroscopic work-hardening curve, given the limitations in differentiating real data. From Fig. 4d and f it can be seen that the $\gamma \rightarrow \alpha'$ is already progressing at this stress with approximately one quarter of the available austenite transformed. The linear increase in the LPS of the remaining austenite indicates an elastic response, i.e. there will be no shear bands present within the austenite phase for martensite to be nucleated. This is a strong argument for the stress-assisted transformation mechanism. Above the yield point of austenite ($\sigma y_{[\gamma]}$), as derived from the stress-strain curve, strains in both the longitudinal and transverse directions tend towards zero as a result of the combination of mechanically induced transformation and significant grain rotation.

The high energy X-ray diffraction experiments allow us not only to follow the load partitioning of the phases, but also the behaviour of specific {hkl} planes of each phase. This is of particular interest for understanding the behaviour of the phases during the mechanically induced transformation. Fig. 4 shows the relative peak intensity of the {hkl} reflections of the austenite phase in (d) the longitudinal and (f) transverse directions. Below the yield point of ferrite, the relative intensities of the individual reflections do not change significantly, whereby above this point, the intensity of all reflections is reduced. Based on Schmid's law, it is possible to determine the stability of the austenite phase based on the grain orientation relative to the loading direction (Schmid and Boas, 1950):

$$\tau = m\sigma = \cos(\lambda)\cos(\varphi)\sigma \tag{4}$$

where the resolved shear stress, τ is related to the applied tensile stress σ by application of the Schmid factor m. This factor is the product of the cosines of the angle between the tensile axis and the {111} slip plane normal (λ) and the angle between the tensile axis and $\langle 110 \rangle$ slip direction (φ). The Schmid factor has been calculated for the planes with the plane normal oriented along the tensile axis, see Table 3. The Schmid factor has been calculated for each of the 12 variations of the {111}$\langle 110 \rangle$ slip family, and the table shows how many of these slip systems have a positive Schmid factor i.e. are active, and how many have the maximum value of the Schmid factor.

From this analysis it can be seen that the {311} planes exhibit the maximum value of the Schmid factor, but on only one of the potential slip systems, despite 10/12 being potentially active. The {200} and {220} have equivalent Schmid factors, but the {200} has more active slip systems, all of which exhibit the highest Schmid factor. This can assist in explaining the slip and rotation behaviour of the relevant austenite plane families. The relative intensities of all planes are largely unaffected up to the yield point of the ferritic matrix, after which the {200} shows the largest change in relative intensity in both the longitudinal and transverse directions, followed by the {311}. The {222} reflection shows the least change, particularly in the transverse direction where the relative intensity remains high throughout the test. This is in good agreement with the accepted theory and previous diffraction studies (Oliver et al., 2002; Asoo et al., 2011; Jimenez-Melero et al., 2011).

3.4. Microstructural development under loading

In order to understand the effect of the mechanically-induced transformation on the work-hardening behaviour, it is also necessary to examine the microstructure of the ferritic matrix at different stages of deformation. Fig. 5 shows the orientation contrast images of the microstructure in (a) the unloaded condition, (e) immediately prior to necking i.e. at UTS and (i) adjacent to the fracture surface at final failure. The initial microstructure shows islands of austenite (γ) plus martensite (α') embedded in the ferrite matrix ($\alpha + \alpha_B$). The crystallographic orientation of the ferrite phase is indicated by the phase contrast. The presence of a clear lath-type substructure in the martensite allows it to be distinguished from the surrounding ferritic matrix.

Deformation in the ferrite is visible at the UTS, both as slip lines visible within the grains and as dark (dislocation rich) regions at the interface with martensite grains. The martensite phase does not appear to have undergone severe deformation at UTS, as can be seen by the relative size of the phase with respect to the original microstructure. This is in stark contrast with the microstructure at final failure, in which it is no longer possible to distinguish the phases due to the very fine sub-structure development as a result of the severe plastic deformation.

Table 3
Calculated Schmid factors (m) for plane families in the austenite phase of TADP800 steel.

Plane (family)	Maximum Schmid factor, m_{max}	Slip systems where $m > 0$	Slip systems where $m = m_{max}$
{111}	0.27	5	5
{200}	0.41	8	8
{220}	0.41	4	4
{311}	0.45	10	1
{222}	0.27	5	5

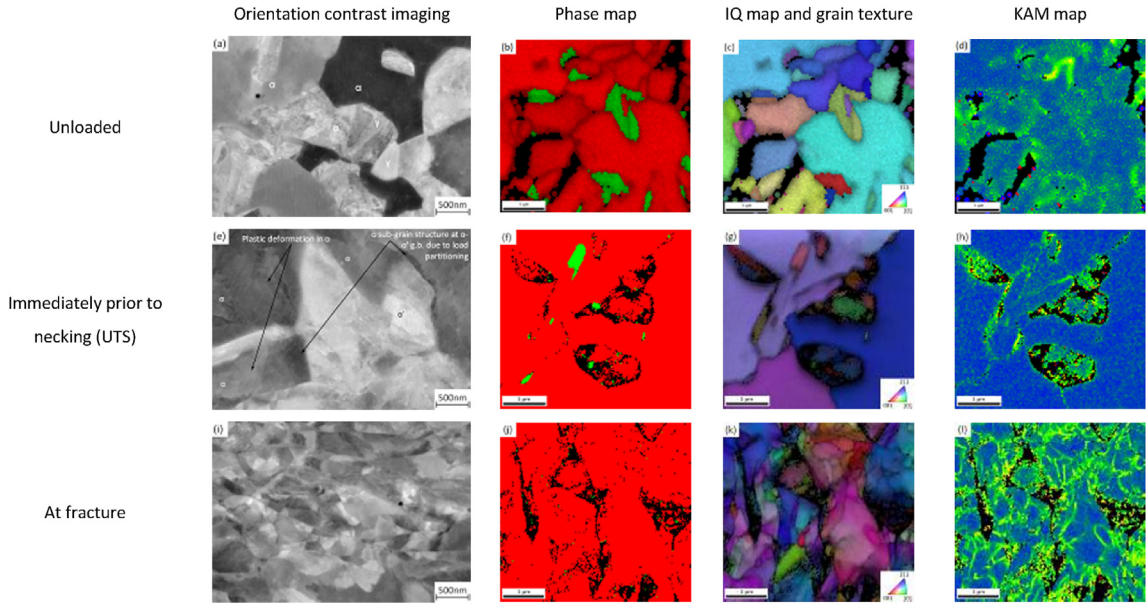| Orientation contrast imaging	Phase map	IQ map and grain texture	KAM map

Fig. 5. (a,e,i) Orientation contrast imaging and maps of (b,f,j) phase fractions of austenite (green), ferrite (red) and mechanically induced martensite (black), (c,g,k) grain orientation and (d,h,l) kernel average misorientation in ferrite, in (a–d) the unloaded condition, (e–h) immediately prior to necking (UTS) and (i–l) at fracture. (For interpretation of the references to colour in this figure legend, the reader is referred to the web version of this article.)

The EBSD analysis of the deformed microstructures gives yet further information about the development of plastic deformation of the phases and, in particular, the transition from uniform to localised plastic deformation. There is only ~1 vol % retained austenite present in the pre-UTS condition, Fig. 5e-h, whilst at final failure there is no austenite left untransformed in the microstructure, Fig. 5i-l. The black regions in the phase map are those which are not indexed due to poor diffraction quality, which is indicative of fresh martensite arising from the mechanically induced transformation (Santofimia et al., 2011; De Knijf et al., 2014). By way of contrast, the indexed (red) portion at the centre of these islands is tempered martensite present after heat-treatment. Some mechanically induced martensite is visible in the EBSD images of the unloaded structure (Fig. 5d) which is due to transformation as a result of the mechanical polishing required for the EBSD analysis (Aarnts et al., 2011). This results in a lower measured fraction of austenite by EBSD technique (<10 vol %) as compared to X-ray diffraction (16 vol %).

Fig. 5c, g, k show the image quality map overlaid with the inverse pole figure (IPF) information at the different deformation steps, in which the development of the ferrite substructure (see Fig. 5i) after the onset of localised necking is clearly shown.

From the KAM maps of the phases in Fig. 5h and l, it can be seen that below the UTS the highest misorientation occurs within the vicinity of the austenite phase, and specifically in the original tempered martensite present in the structure. The surrounding ferrite matrix does not show significant misorientation within the grains themselves, but rather at the grain boundaries. At final failure, the KAM maps reveal a much more extensive deformation network in the ferrite grains surrounding the mechanically-induced martensite (black regions) as a result of the extensive plastic deformation in this phase.

3.5. Interaction between γ-α′ transformation and work hardening behaviour

Based on the experimental evidence presented in previous sections, it is clear that yielding does not occur in all of the constituent phases simultaneously. By examining the relationship between the mechanically induced transformation and the macroscopic work-hardening rate, we can understand the influence of the local mechanical properties on the global plasticity. Fig. 6 shows the progression of the mechanically induced transformation and the work hardening rate, $\Theta = d\sigma/d\varepsilon$, as a function of the nominal equivalent stress (Mecking and Kocks, 1981). Inflections in this curve, as deduced from the second hardening derivative ($d^2\sigma/d\varepsilon^2$) and represented by open grey diamonds in Fig. 6, reveal the contributions of each phase to the work-hardening rate.

According to van Liempt and Sietsma (2016) the pre-yield work-hardening behaviour (Θ^a) of the matrix can be described by the reversible motion of dislocations as described by the following equation:

$$\Theta^a = \frac{M^2 E s^3 \sqrt{1-s^2}}{\rho L^2 (1+v)\left(s - \arcsin(s)\sqrt{1-s^2}\right)} \qquad (5)$$
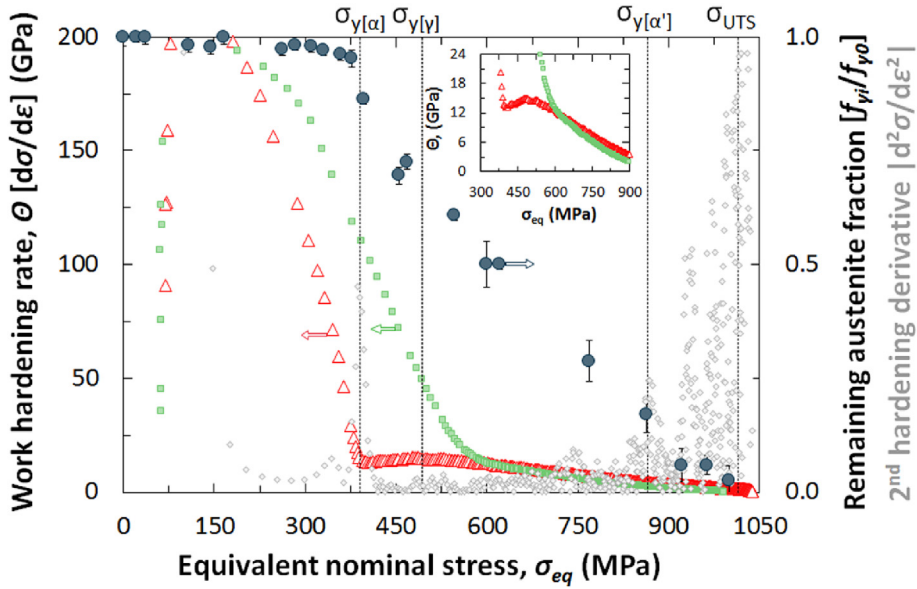
Fig. 6. Relationship between the mechanically induced transformation of austenite to martensite (blue circles) and the work hardening rate of the TRIP-assisted DP steel (red triangles) to the nominal stress. The work hardening rate of DP800 is shown for comparison (green squares). The yield stresses of ferrite ($\sigma_{y[\alpha]}$), austenite ($\sigma_{y[\gamma]}$) and martensite ($\sigma_{y[\alpha']}$) phases in the TADP steel are calculated from the second derivative of the work-hardening curve (grey diamonds), and are indicated along with the ultimate tensile strength (σ_{UTS}) of this material by the vertical dashed lines. (For interpretation of the references to colour in this figure legend, the reader is referred to the web version of this article.)

where M is the Taylor factor, E is the elastic modulus, ν is the Poisson ratio and s is the normalised stress parameter being the ratio of the applied stress to the critical stress, σ_c for generation of dislocations from a Frank-Read source. ρ is the dislocation density and L is the dislocation segment length. The combined parameter ρL^2 is a quantitative description of the dislocation structure in the material.

The yield stress can be determined by the intersection of the pre-yield region with the Stage-III hardening (Θ^{post}) defined by Mecking and Kocks (1981):

$$\Theta^{post} = \frac{1}{2}(\alpha MGbU - \Omega\sigma_w) \tag{6}$$

Where U and Ω are the dislocation storage rate and dynamic recovery rate, respectively. G is the elastic shear modulus, b is the Burger's vector and σ_w is the work-hardening contribution to the flow stress. M is the Taylor factor and α is a material factor related to the dislocation density and distribution.

This model can be used to understand the work-hardening behaviour of the materials in question, as shown in Fig. 6. Given the generally accepted value of the elastic modulus of steel of 200 GPa, the maximum work-hardening rate in the pre-yield regime of a purely elastic material would achieve this value, with a sharp drop at the yield stress. In the early pre-yield regime, the maximum work-hardening rate of both materials coincides with the value for the elastic modulus. From Eq. (5) it can therefore be deduced that the dislocation structure in both materials is equivalent, given also the fact that the grain size and morphology of the ferrite phase of both materials is also the same and that the work-hardening rate of both materials deviates from the pure elastic condition at the same value of applied stress.

The TADP material shows a much steeper drop in work-hardening rate which can be explained as the result of reversible dislocation glide. The sharp transition from softening to work-hardening at a single stress demonstrates that the dislocation structure is fairly uniform and that the yield stress approaches the theoretical value for σ_c. The diffraction data shows that the transformation from austenite to martensite does not occur in this pre-yield region and therefore the transformation itself cannot contribute to the dislocation structure of the matrix phase. This is further illustrated by the work-hardening behaviour of the DP grade in the same region.

The DP deviates from pure elastic behaviour at the same applied stress as the TADP but due to the influence of the hard martensite phase (which is present in much higher quantities in the initial microstructure), the ferrite phase is subjected to non-uniform deformation. This requires the generation of geometrically necessary dislocations (GNDs) within the ferrite phase. Vegter and van Liempt (2011) have shown that the consequence of the formation of GNDs is a short range increase of local dislocations in the softer phase leading to a back stress in the soft-phase and a forward stress in the hard phase. Equalisation of these stresses due to load partitioning leads to an apparently higher value for the yield stress for the DP

material, although it can be seen from Fig. 6 that there is no distinct transition from pre-to post-yield behaviour in this material.

The slope of the Stage-III hardening is a function of the work-hardening parameter Ω in Eq. (6). Since we have already determined that the dislocation structure in the both materials is equivalent, it follows that the parameters describing the dislocation behaviour ($\alpha MGbU$) are also the same for both materials. From Fig. 6 it can be seen that the slopes of Stage-III hardening of both materials is the same, thus Ω is equal. The difference in post-yield work-hardening can thus only be attributed to an increase in the work-hardening contribution, σ_w as a result of the austenite to martensite transformation.

Upon reaching the yield point, activation of Frank-Read sources requires the ferrite phase to undergo hardening and signals the onset of the austenite to martensite transformation. Ferrite is thus the first phase to undergo deformation, with clear anelastic behaviour in the pre-yield region. Given that there is no transformation of austenite in this region and that the yield point of austenite is clearly higher than that of ferrite (see Section 3.3), it follows that mechanically induced transformation begins after the onset of matrix yielding and leads to a temporary increase in work-hardening. Due to the need to accommodate the volumetric expansion accompanied by the transformation, dislocations must be created in the surrounding tempered martensite. Accommodation of the local volumetric change is thereby accompanied by an increase in local microscopic internal stresses, the so-called Greenwood-Johnson effect (Greenwood and Johnson, 1965), stimulating plastic flow in the weaker phase, thereby leading to macroscopic hardening.

This is followed by yielding of the austenite phase (see Fig. 4b) and a reduction of the work-hardening rate of the ferrite phase. Beyond this point, the reduction in work-hardening rate in ferrite in the TADP is slower than in the comparable ferrite in the dual phase steel due to the extra work required for the accommodation of the $\gamma \to \alpha'$ transformation. At the yield point of the martensite phase there is still some residual austenite which offset the softening in this phase. It is also apparent that whilst the original tempered martensite has deformed prior to the UTS, yielding in the mechanically induced (fresh) martensite has not significantly occurred at this point, as discussed in Section 3.4. Diffuse instability (necking) occurs, at $\sigma = \Theta$, only after all of the austenite has transformed and is rapidly followed by failure. Between the UTS and final failure, the fresh martensite has significantly co-deformed with the matrix phase.

The same mechanism can be used to interpret the data presented by Jacques and Han. By comparing the stress-strain response with the acoustic emission signal (Jacques et al., 2001), it can be seen that the drop in acoustic emission attributed to the onset of austenite transformation is commensurate with the end of the yield plateau. The transformed martensite fraction measured by (Han et al. 2004, Fig. 4) remains at its initial level until above 0.1 true strain, at which point all of the steels under investigation are above the nominal yield point (the steels exhibit continuous yielding behaviour) (Han et al., 2004; Fig. 5). Further datasets of the interaction between matrix yielding and mechanically induced transformation are provided in the supplementary data. It should be noted that these datasets are based on ex-situ measurement of the retained austenite fraction. Future in-situ synchrotron experiments are planned to further verify the hardening model proposed in this paper.

Finally, the massive plastic deformation of the martensite phase above the UTS should serve as a cautionary note to treating martensite as a purely elastic phase, such as in Ma and Hartmaier (2015). Although this is correct up to the uniform strain in a uniaxial tensile test, in real world forming operations e.g. deep drawing the strains experienced can be up to twice those of the uniaxial strain, with plastic deformation of martensite as a result which must be taken into account for the model to be realistic.

4. Conclusions

We have assessed the effect of retained austenite on the work hardening behaviour in a high strength, TRIP-assisted Dual Phase steel. For this purpose, we have performed in situ high energy X-ray diffraction experiments at a synchrotron source during uniaxial loading. The results have been supported by ex situ X-ray diffraction experiments, and also by the characterisation of the local microstructure using scanning electron microscopy. The progression of the mechanically induced transformation from austenite to martensite, load partitioning between the phases and the effects on the mechanical properties of the material were examined and discussed.

The main conclusions of this study are: (1) the mechanically induced transformation does not begin until the onset of matrix yielding and leads to macroscopic hardening due to accommodation of the transformation strain; (2) plastic deformation of the non-transformed austenite does not significantly occur either prior to, or at the onset of, the phase transformation, and austenite yielding coincides with a maximum in the work hardening rate; (3) transformation of austenite to martensite is stress-assisted and the work required offsets the softening in ferrite leading to increased ductility at higher stress levels; (4) yielding of the mechanically induced martensite does not occur until the austenite phase has completely transformed. Plastic deformation of martensite is quickly followed by local plastic instability leading to necking and ultimate failure of the material.

Author contributions

Ex-situ tensile experiments and XRD analysis were performed by EHA, BLE and DNH; EBSD analysis by MK and BLE. The manuscript was prepared by BLE, EJ-M, EHA and PDL.

Data statement

A representative sample of research data from the experiments along with the plot data for the graphs in this manuscript is provided in supplementary material [http://dx.doi.org/10.17632/mx7p29b72t.3]. The underlying data is not provided online due to its size (around 0.5TB).

Acknowledgements

References

Aarnts, M.P., Rijkenberg, R.A., Twisk, F.A., 2011. Microstructural Quantification of Multi-phase Steels (Micro-quant). European Commission. http://dx.doi.org/10.2777/83656.

Adams, J.J., Agosta, D.S., Leisure, R.G., Ledbetter, H., 2006. Elastic constants of monocrystal iron from 3 to 500 K. J. Appl. Phys. 100, 113530. http://dx.doi.org/10.1063/1.2365714.

Asoo, K., Tomota, Y., Harjo, S., Okitsu, Y., 2011. Tensile behavior of a TRIP-aided ultra-fine grained steel studied by neutron diffraction. ISIJ Int. 51, 145–150. http://dx.doi.org/10.2355/isijinternational.51.145.

Bergström, Y., 1970. A dislocation model for the stress-strain behaviour of polycrystalline α-Fe with special emphasis on the variation of the densities of mobile and immobile dislocations. Mater. Sci. Eng. 5, 193–200. http://dx.doi.org/10.1016/0025-5416(70)90081-9.

Bhadeshia, H.K.D.H., Edmonds, D.V., 1979. The bainite transformation in a silicon steel. Metall. Trans. A 10, 895–907.

Blondé, R., Jimenez-Melero, E., Zhao, L., Wright, J.P., Brück, E., van der Zwaag, S., van Dijk, N.H., 2012. High-energy X-ray diffraction study on the temperature-dependent mechanical stability of retained austenite in low-alloyed TRIP steels. Acta Mater. 60, 565–577. http://dx.doi.org/10.1016/j.actamat.2011.10.019.

Bruker AXS GmbH, 2009. TOPAS, 2009. General Profile and Structure Analysis Software for Powder Diffraction Data.

Cherkaoui, M., Berveiller, M., Lemoine, X., 2000. Couplings between plasticity and martensitic phase transformation: overall behavior of polycrystalline TRIP steels. Int. J. Plast. 16, 1215–1241. http://dx.doi.org/10.1016/S0749-6419(00)00008-5.

De Knijf, D., Petrov, R., Föjer, C., Kestens, L.A.I., 2014. Effect of fresh martensite on the stability of retained austenite in quenching and partitioning steel. Mater. Sci. Eng. A 615, 107–115. http://dx.doi.org/10.1016/j.msea.2014.07.054.

Ehrhardt, B., Gerber, T., Schaumann, T.W., 2004. Approaches to microstructural design of TRIP and TRIP aided cold rolled high strength steels. In: International Conference on Advanced High Strength Sheet Steels for Automotive Applications. AIST, Winter Park, CO, USA, pp. 39–50.

Ennis, B.L., Jimenez-Melero, E., Mostert, R., Santillana, B., Lee, P.D., 2016. The role of aluminium in chemical and phase segregation in a TRIP-assisted dual phase steel. Acta Mater. 115, 132–142. http://dx.doi.org/10.1016/j.actamat.2016.05.046.

Fischer, F.D., Reisner, G., Werner, E., Tanaka, K., Cailletaud, G., Antretter, T., 2000. A new view on transformation induced plasticity (TRIP). Int. J. Plast. 16, 723–748.

Franz, G., Abed-Meraim, F., Berveiller, M., 2013. Strain localization analysis for single crystals and polycrystals: towards microstructure-ductility linkage. Int. J. Plast. 48, 1–33. http://dx.doi.org/10.1016/j.ijplas.2013.02.001.

Geijselaers, H.J.M., Perdahcıoğlu, E.S., 2009. Mechanically induced martensitic transformation as a stress-driven process. Scr. Mater. 60, 29–31. http://dx.doi.org/10.1016/j.scriptamat.2008.08.043.

Gomez, M., Garcia, C.I.I., Haezebrouck, D.M.D.M., DeArdo, A.J.A.J., 2009. Design of composition in (Al/Si)-alloyed TRIP steels. ISIJ Int. 49, 302–311. http://dx.doi.org/10.2355/isijinternational.49.302.

Greenwood, G.W., Johnson, R.H., 1965. The deformation of metals under small stresses during phase transformations. Proc. R. Soc. A Math. Phys. Eng. Sci. 283, 403–422. http://dx.doi.org/10.1098/rspa.1965.0029.

Hammersley, A.P., Svensson, S.O., Hanfland, M., Fitch, A.N., Hausermann, D., 1996. Two-dimensional detector software: from real detector to idealised image or two-theta scan. High. Press. Res. 14, 235–248. http://dx.doi.org/10.1080/08957959608201408.

Han, H.N., Lee, C.G., Oh, C.-S., Lee, T.-H., Kim, S.-J., 2004. A model for deformation behavior and mechanically induced martensitic transformation of metastable austenitic steel. Acta Mater. 52, 5203–5214. http://dx.doi.org/10.1016/j.actamat.2004.07.031.

Han, H.N., Lee, C.G., Suh, D.-W., Kim, S.-J., 2008. A microstructure-based analysis for transformation induced plasticity and mechanically induced martensitic transformation. Mater. Sci. Eng. A 485, 224–233. http://dx.doi.org/10.1016/j.msea.2007.08.022.

Hofmann, H., Matissen, D., Schaumann, T.W., 2009. Advanced cold-rolled steels for automotive applications. Steel Res. Int. 80, 22–28. http://dx.doi.org/10.2374/SRI08SP113.

Jacques, P., Furnémont, Q., Mertens, A., Delannay, F., 2001. On the sources of work hardening in multiphase steels assisted by transformation-induced plasticity. Philos. Mag. A 81, 1789–1812. http://dx.doi.org/10.1080/01418610108216637.

Jimenez-Melero, E., van Dijk, N.H., Zhao, L., Sietsma, J., Offerman, S.E., Wright, J.P., van der Zwaag, S., 2007. Characterization of individual retained austenite grains and their stability in low-alloyed TRIP steels. Acta Mater. 55, 6713–6723. http://dx.doi.org/10.1016/j.actamat.2007.08.040.

Jimenez-Melero, E., van Dijk, N.H., Zhao, L., Sietsma, J., Wright, J.P., van der Zwaag, S., 2011. In situ synchrotron study on the interplay between martensite formation, texture evolution and load partitioning in low-alloyed TRIP steels. Mater. Sci. Eng. A 528, 6407–6416. http://dx.doi.org/10.1016/j.actamat.2007.08.040.

Khan, A.S., Baig, M., Choi, S.-H., Yang, H.-S., Sun, X., 2012. Quasi-static and dynamic responses of advanced high strength steels: experiments and modeling. Int. J. Plast. 30–31, 1–17. http://dx.doi.org/10.1016/j.ijplas.2011.08.004.

Kobayashi, J., Song, S.-M.S.M., Sugimoto, K., 2012. Microstructure and retained austenite characteristics of ultra-high strength TRIP-aided martensitic steels. ISIJ Int. 52, 1124–1129. http://dx.doi.org/10.2355/isijinternational.52.1124.

Kubler, R.F., Berveiller, M., Buessler, P., 2011. Semi phenomenological modelling of the behavior of TRIP steels. Int. J. Plast. 27, 299–327. http://dx.doi.org/10.1016/j.ijplas.2010.05.002.

Leblond, J.B., Devaux, J.C., Devaux, J.C., 1989. Mathematical modelling of transformation plasticity in steels I: case of ideal-plastic phases. Int. J. Plast. 5, 551–572. http://dx.doi.org/10.1016/0749-6419(89)90001-6.

Ma, A., Hartmaier, A., 2015. A study of deformation and phase transformation coupling for TRIP-assisted steels. Int. J. Plast. 64, 40–55. http://dx.doi.org/10.1016/j.ijplas.2014.07.008.

Mahnken, R., Schneidt, A., Antretter, T., 2009. Macro modelling and homogenization for transformation induced plasticity of a low-alloy steel. Int. J. Plast. 25, 183–204. http://dx.doi.org/10.1016/j.ijplas.2008.03.005.

Matlock, D.K., Speer, J.G., 2008. Third generation of AHSS: microstructure design concepts. In: Haldar, A., Suwas, S., Bhattacharjee, D. (Eds.), Microstructure and Texture in Steels and Other Materials. Springer, Jamshedpur, India, pp. 185–205.

Mazinani, M., Poole, W.J., 2007. Effect of martensite plasticity on the deformation behavior of a low carbon dual-phase steel. Metall. Mater. Trans. A 38, 328–339. http://dx.doi.org/10.1007/s11661-006-9023-3.

Mecking, H., Kocks, U.F., 1981. Kinetics of flow and strain-hardening. Acta Metall. 29, 1865–1875. http://dx.doi.org/10.1016/0001-6160(81)90112-7.

Miyamoto, G., Shibata, A., Maki, T., Furuhara, T., 2009. Precise measurement of strain accommodation in austenite matrix surrounding martensite in ferrous alloys by electron backscatter diffraction analysis. Acta Mater. 57, 1120–1131. http://dx.doi.org/10.1016/j.actamat.2008.10.050.

NIST, 2010. Lanthanum Hexaboride Powder Line Position and Line Shape Standard for Powder Diffraction (CTLG No. SRM 660b (2010).). National Institute of Standards and Technology, U.S. Department of Commerce, Gaithersburg, MD, USA, MD, USA.

Oliver, E.C., Withers, P.J., Daymond, M.R., Ueta, S., Mori, T., 2002. Neutron-diffraction study of stress-induced martensitic transformation in TRIP steel. Appl. Phys. A 74, 1143–1145. http://dx.doi.org/10.1007/s003390201555.

Oliver, S., Jones, T.B., Fourlaris, G., 2007. Dual phase versus TRIP strip steels: microstructural changes as a consequence of quasi-static and dynamic tensile testing. Mater. Charact. 58, 390–400. http://dx.doi.org/10.1016/j.matchar.2006.07.004.

Olson, G.B., Cohen, M., 1982. Stress-assisted isothermal martensitic transformation: application to TRIP steels. Metall. Trans. A 13, 1907–1914. http://dx.doi.org/10.1007/BF02645934.

Olson, G.B., Cohen, M., 1975. Kinetics of strain-induced martensitic nucleation. Metall. Trans. A 6, 791–795. http://dx.doi.org/10.1007/BF02672301.

Patel, J.R., Cohen, M., 1953. Criterion for the action of applied stress in the martensitic transformation. Acta Metall. 1, 531–538. http://dx.doi.org/10.1016/0001-6160(53)90083-2.

Perdahcıoğlu, E.S., Geijselaers, H.J.M., 2012. A macroscopic model to simulate the mechanically induced martensitic transformation in metastable austenitic stainless steels. Acta Mater. 60, 4409–4419. http://dx.doi.org/10.1016/j.actamat.2012.04.042.

Ramazani, A., Mukherjee, K., Schwedt, A., Goravanchi, P., Prahl, U., Bleck, W., 2013. Quantification of the effect of transformation-induced geometrically necessary dislocations on the flow-curve modelling of dual-phase steels. Int. J. Plast. 43, 128–152. http://dx.doi.org/10.1016/j.ijplas.2012.11.003.

Santofimia, M.J., Zhao, L., Petrov, R., Kwakernaak, C., Sloof, W.G., Sietsma, J., 2011. Microstructural development during the quenching and partitioning process in a newly designed low-carbon steel. Acta Mater. 59, 6059–6068. http://dx.doi.org/10.1016/j.actamat.2011.06.014.

Savitzky, A., Golay, M.J.E., 1964. Smoothing and differentiation of data by simplified least squares procedures. Anal. Chem. 36, 1627–1639. http://dx.doi.org/10.1021/ac60214a047.

Schmid, E., Boas, W., 1950. Plasticity of Crystals with Special Reference to Metals. F.A. Hughes & Co. Ltd, London, UK.

Scott, C.P., Drillet, J., 2007. A study of the carbon distribution in retained austenite. Scr. Mater. 56, 489–492. http://dx.doi.org/10.1016/j.scriptamat.2006.11.033.

The International Organisation for Standardisation (ISO), 2009. Metallic Materials - Tensile Testing - Part 1: Method of Testing at Ambient Temperature. ISO 6892–1 (Geneve, Switzerland).

Van Dijk, N.H.H., Butt, A.M., Zhao, L., Sietsma, J., Offerman, S.E., Wright, J.P., Van Der Zwaag, S., 2005. Thermal stability of retained austenite in TRIP steels studied by synchrotron X-ray diffraction during cooling. Acta Mater. 53, 5439–5447. http://dx.doi.org/10.1016/j.actamat.2005.08.017.

van Liempt, P., 1994. Workhardening and substructural geometry of metals. J. Mater. Process. Technol. 45, 459–464.

van Liempt, P., Sietsma, J., 2016. A physically based yield criterion I. Determination of the yield stress based on analysis of pre-yield dislocation behaviour. Mater. Sci. Eng. A 662, 80–87. http://dx.doi.org/10.1016/j.msea.2016.03.013.

Vegter, H., van Liempt, P., 2011. Modelling of workhardening of multiphase steels. Steel Res. Int. 824–829.

Wolff, M., Böhm, M., Dalgic, M., Hüßler, I., 2008. Evaluation of models for TRIP and stress-dependent transformation behaviour for the martensitic transformation of the steel 100Cr6. Comput. Mater. Sci. 43, 108–114. http://dx.doi.org/10.1016/j.commatsci.2007.07.040.